

Smaller is stronger: The effect of strain hardening

R. Maaß^a, S. Van Petegem^a, Duancheng Ma^b, Julien Zimmermann^a, Daniel Grolimund^a, Franz Roters^b, H. Van Swygenhoven^{a,*}, Dierk Raabe^b

^a Paul Scherrer Institute, CH-5232 Villigen, Switzerland

^b Max-Planck-Institut für Eisenforschung, Max-Planck-Str. 1, 40237 Düsseldorf, Germany

Received 4 June 2009; received in revised form 4 August 2009; accepted 12 August 2009

Available online 11 September 2009

Abstract

Single-crystal face-centered cubic metal pillars synthesized using a focused ion beam are reported to be stronger when compressed in smaller volumes. Using in situ Laue diffraction and crystal plasticity simulations it is shown that plastic deformation is initially controlled by the boundary constraints of the microcompression tests, followed by classical crystal plasticity for uniaxial compression. Taking the stress at which the change between the two modes occurs as strength of the pillar instead of the flow stress at a fixed amount of strain, the “smaller is stronger” trend is considerably reduced, if not eliminated, and what remains is a size dependence in strain hardening. The size-dependent increase in flow stress is a result of the early activation of multiple slip systems and thus the evolution of the microstructure during compression.

© 2009 Acta Materialia Inc. Published by Elsevier Ltd. All rights reserved.

Keywords: Microcompression; Plastic deformation; Strain gradient; Single crystal; Strain hardening

1. Introduction

The development of a microcompression technique allowing compression of pillars with diameters below 10 μm has opened new routes for investigating the mechanical behavior of small volumes [1]. Such a technique is important for studying material properties for microtechnological applications [2–4], but the technique is also very promising for the investigation of small irradiated volumes or individual phases in complex advanced alloys. Microcompression revealed an increase in strength for single-crystal pillars when pillar diameters are reduced below 10 μm [1,5–8]. The “smaller is stronger” trend for single crystals has perplexed materials scientists, because it does not fit into classical crystal plasticity where the strength of a single crystal does not depend on its size but rather on the geometrically predicted dislocation slip system(s)

for which the resolved shear stress is the highest [9]. The strength or resistance to permanent strain is expressed by the yield stress or the onset of percolative slip and is usually defined as the flow stress at 0.2% plastic strain [10]. When a single crystal is deformed to larger plastic strains, other mechanisms come into play such as dislocation interactions resulting in entanglements and self-organization mechanism forming crystallographic substructures. During this microstructural evolution, the metal hardens, i.e. the flow stress increases [11]. At very large strains a polycrystal composed of grains with different orientations is formed. The yield stress of a polycrystal is well known to increase with the inverse square root of the grain size which is ascribed to the piling up of dislocations at the interfaces between adjacent grains [12,13].

Because of the large stress–strain scatter observed in the initial stage of plastic flow in a microcompression test, the flow stress at a relative large amount of total strain (usually 5% or more) is used to demonstrate the “smaller is stronger” trend [1,5,6,14–16]. Since elastic strains in pure face-centered cubic (fcc) metals are well below 1% total strain

* Corresponding author. Tel.: +41 56 3102931; fax: +41 56 3103131.

E-mail addresses: helena.vs@psi.ch, helena.vanswygenhoven@psi.ch (H. Van Swygenhoven).

[17], the origin of the remaining total strain has to be explored to justify the 5% criterion.

X-ray diffraction has been used for local probing of the microstructure and has been demonstrated to allow the spatial resolution of local strains within dislocation cells [18,19], the observation of grain rotation during plastic deformation [20] and the existence of dilatational strain gradients in Mo-alloy pillars of 550 nm diameter [21]. Here, polychromatic microfocused Laue diffraction was performed in situ during microcompression, as this technique elucidates the dynamics of the self-organization process of dislocations leading to the formation of subgrain structures [22]. Laue diffraction performed with a micron-sized beam on micropillars synthesized using a focused ion beam (FIB) has demonstrated the presence of strain gradients and defects prior to deformation [23–25]. Performed in situ, the technique has demonstrated the role a pre-existing strain gradient can play on the selection of the activated slip planes at large total strains [26], and also the formation of rotational gradients at high strains [27]. The present study focuses on lattice rotations captured in situ by tracking the path of the Laue spot at low total strains, with the goal of approaching as close as possible to the onset of percolative slip. The in situ Laue method is combined with crystal plasticity finite-element simulations, allowing us to study the influence of the boundary conditions on slip activation.

2. Materials and methods

2.1. Analysis of Laue lattens

A Laue diffraction pattern taken with a polychromatic X-ray beam is characterized by individual spots, each related to a different hkl-family. The position of the Laue spots depends on the crystal orientation and the shape of the unit cell. Therefore any crystal rotation and/or change in the shape of the unit cell will result in peak movements. For Laue analysis it is practical to decompose the strain tensor into a deviatoric and a hydrostatic (isotropic dilatation) strain tensor [28,29]. Isotropic changes in the crystal unit cell do not change the position of the Laue reflections. Therefore, to determine the lattice parameter and the hydrostatic dilatation strain tensor, energy scans with a monochromatic X-ray beam are needed. On the other hand, deviatoric strains result in changes in the shape of the unit cell and therefore result in reflections that are slightly offset from their unstrained positions. Continuous streaking of Laue reflections obtained from polychromatic X-rays is therefore related to the presence of deviatoric strain gradients in the illuminated volume. Such gradients are often—but not necessarily—related to an excess dislocation content of one type. Indeed, an elastic tetragonal distortion of the unit cell will also cause deviatoric strains without the presence of dislocations. Discontinuous streaking points towards misorientations and is usually related to

the presence of misorientations dislocation walls, forming geometrically necessary boundaries [30].

In this paper polychromatic Laue diffraction is applied and therefore the observed peak streaking is caused by deviatoric gradients. During in situ deformation, the movement of Laue peaks is interpreted as crystal rotation. In this way the path of the spots can be directly linked to a specific active slip system using the rotational Taylor model [31,32]. From the collective motion of all the Laue spots, the rotation of the compression axis can be quantified [33].

2.2. Investigated material

In situ tests were conducted on Au samples being oriented for single ($\langle 1\ 2\ 3 \rangle$, $\langle 3\ 4\ 6 \rangle$) and double slip ($\langle 0\ 0\ 1 \rangle$), and on single slip oriented Ni ($\langle 1\ 2\ 3 \rangle$). Both the $\langle 1\ 2\ 3 \rangle$ - and $\langle 0\ 0\ 1 \rangle$ -oriented Au, and the $\langle 1\ 2\ 3 \rangle$ -oriented Ni pillars were synthesized from a bulk single crystal that was obtained from the melt by the Czochralski method and provided by Mateck. The $\langle 3\ 4\ 6 \rangle$ -oriented samples were prepared from a well-annealed Au foil, of which more details can be found in the online material of Ref. [26]. It has previously been shown that the $3\ \mu\text{m}$ Au($3\ 4\ 6$)-pillar contained a twin [24]. All Au pillars were cut out from the bulk crystal using FIB, employing the annular milling procedure [6], providing a typical mean sidewall taper of $\sim 2.3^\circ$ and aspect ratios ranging between 1.3 and 2.2 if the diameter is determined at half the pillar height. Au pillars with diameters between 2 and $10\ \mu\text{m}$ were investigated. The $8.0\ \mu\text{m}$ (A and B) and one $4.0\ \mu\text{m}$ Ni pillars with an aspect ratio of 2.8 were prepared by the lathe FIB-milling technique [34] by M.D. Uchic and have no taper. In total 13 pillars were investigated, for which the diameter and initial compression axis orientation can be found in the first two columns of Table 2 below. Knowing the pillar axis orientation derived from the diffraction data enabled the Schmid factors (SFs) for each slip to be calculated. Table 1 provides the 12 SFs obtained for both the $\langle 1\ 2\ 3 \rangle$ -oriented Au and Ni pillars. Small differences in SF between Au and Ni are due to small differences in alignment of the bulk crystals on the sample holder.

Table 1
Schmid factors (SF) for Au[1 2 3] and Ni[1 2 3].

Au			Ni		
Nr.	Slip system no.	SF	Nr.	Slip system no.	SF
1	(-1 1 1)[1 0 1]	0.472	1	(-1 1 1)[1 0 1]	0.475
2	(1 1 1)[-1 0 1]	0.365	2	(1 1 1)[-1 0 1]	0.374
3	(-1 1 1)[1 1 0]	0.340	3	(-1 1 1)[1 1 0]	0.349
4	(1 -1 1)[0 1 1]	0.302	4	(1 -1 1)[0 1 1]	0.281
5	(1 1 1)[-1 1 0]	0.194	5	(1 1 1)[-1 1 0]	0.195
6	(1 1 1)[0 -1 1]	0.174	6	(1 1 1)[0 -1 1]	0.179
7	(1 -1 1)[1 1 0]	0.171	7	(1 -1 1)[1 1 0]	0.160
8	(-1 1 1)[0 -1 1]	0.132	8	(-1 1 1)[0 -1 1]	0.126
9	(1 -1 1)[-1 0 1]	0.127	9	(1 -1 1)[-1 0 1]	0.121
10	(-1 -1 1)[0 1 1]	0.025	10	(-1 -1 1)[0 1 1]	0.024
11	(-1 -1 1)[1 0 1]	0.020	11	(-1 -1 1)[1 0 1]	0.019
12	(-1 -1 1)[-1 1 0]	0.005	12	(-1 -1 1)[-1 1 0]	0.005

Table 2
Stresses (σ) at various strain (ε) values compared to “Laue yield for Au and Ni”.

Pillar diameter (μm)		Orientation $\langle u v w \rangle$	Laue yield (MPa)	(σ and ε) (%)	Rotation ($^\circ$)	σ at 5% ε^a (MPa)
2.2		$\langle 1\ 2\ 3 \rangle$	42	1.5	0.17	57
2.3		$\langle 1\ 2\ 3 \rangle$	41	0.2	0.06	62
2.4		$\langle 1\ 2\ 3 \rangle$	48	1.9	0.16	71
3.2		$\langle 1\ 2\ 3 \rangle$	54	0.6	0.05	62
4.5		$\langle 1\ 2\ 3 \rangle$	36	2.2	0.15	50
2.4		$\langle 0\ 0\ 1 \rangle$	46	1.4	0.11	64
5.1		$\langle 0\ 0\ 1 \rangle$	33	2.3	0.11	46
3.6		$\langle 3\ 4\ 6 \rangle$	46	2.3	0.49	52
4.6		$\langle 3\ 4\ 6 \rangle$	28	0.5	–	75
10.0		$\langle 3\ 4\ 6 \rangle$	27	1.2	0.10	52
8.0	Ni(A)	$\langle 1\ 2\ 3 \rangle$	100	0.8	0.13	115
8.0	Ni(B)	$\langle 1\ 2\ 3 \rangle$	86	1.1	0.33	133
4.0	Ni	$\langle 1\ 2\ 3 \rangle$	96	0.3	0.42	141

^a As used in Ref. [6].

Prior to deformation, all pillars were investigated with respect to their initial microstructure. From the peak shape of the Laue spots it is clear that all Au peaks originating from single slip oriented samples contain deviatoric strain gradients. Note that deviatoric strain gradients were not observed in as-prepared Mo pillars which were synthesized without the use of FIB [21]. On the other hand, by applying energy scans, a dilatational strain gradient was observed in the Mo wires between the embedded and the free-standing part of the pillar. The 3.2 and 2.3 μm Au $\langle 1\ 2\ 3 \rangle$ pillars both have additionally a misorientation at the pillar base that in the case of the 3.2 μm pillar extends well into the pillar, very much conforming with the results shown in Ref. [24]. Both the Ni-B pillar and the 4 μm Ni pillar contain a pre-existing misorientation, whereas the shape of the peaks in Ni-A do not provide evidence of any strain gradient along the entire vertical pillar axis [24]. In the two multiple slip oriented Au pillars no significant initial defects could be detected.

2.3. In situ microcompression

The combination of white beam Laue diffraction and microcompression was developed to study the evolving microstructure in micropillars during their deformation. The experiment is based on a custom designed microcompression device (MCD), which uses a standard 1D Triboscope transducer from Hysitron Inc. for force and displacement readout. During in situ testing at the MicroXAS beam line of the Swiss Light Source (SLS), two high-resolution microscopes are used to monitor the alignment, compression anvil approach, and the compression experiment in two perpendicular planes, which is a significant advantage compared to conventional microcompression. X-ray focusing is carried out by a set of Kirkpatrick–Baez mirrors, yielding in this study a beam width (full width at half maximum) in the focal plane of 2 μm (Au) and 1 μm (Ni). A charge-coupled device (CCD) detector is positioned in a Laue transmission geom-

etry at typical sample to detector distances of around 50 mm. The system resolution was determined with diffraction data taken from a Si wafer, and resulted in a resolution of $\sim 0.06^\circ$, which incorporated both the instrumental broadening function and the beam divergence. Emitted fluorescence light from the sample is detected by a single-element analogue X-ray acquisition system, allowing the reconstruction of the sample position in experimental coordinates. This method unambiguously determines the sample position relative to the microfocused X-ray beam. Further details on the experimental set-up can be found in the online material of Ref. [26].

The stress–strain curves obtained during microcompression show typically a rather low modulus, as is also the case in all other published data for fcc metals. To check the stiffness of the machine, calibration indents with a standard Berkovich indentation tip have been performed on quartz, resulting in an indentation modulus of 76 GPa, showing a good agreement with the literature [35]. It has to be mentioned that strain measurements with a transducer are very sensitive to thermal drift. Indentation software programs usually allow for automatic correction for such a drift. Here no such automatic correction could be applied because of the long duration of the in situ compression tests. Correction factors are usually very small (of the order of $\pm 0.1\ \text{nm s}^{-1}$) but nevertheless can have a significant influence on the apparent modulus. For instance, applying a correction factor of $-0.06\ \text{nm s}^{-1}$ to a flow curve from the present work (Fig. 1e) yields a modulus of 19 GPa, which an acceptable value for an uniaxial test on a material with a modulus of 40–70 GPa. All compression experiments were conducted in a load-controlled mode with loading rates between 1 and 3 $\mu\text{N s}^{-1}$.

2.4. Crystal plasticity finite-element simulations

The finite-element method allows one to treat complex boundary conditions in materials mechanics. The concept consists in dividing continuum space into small domains

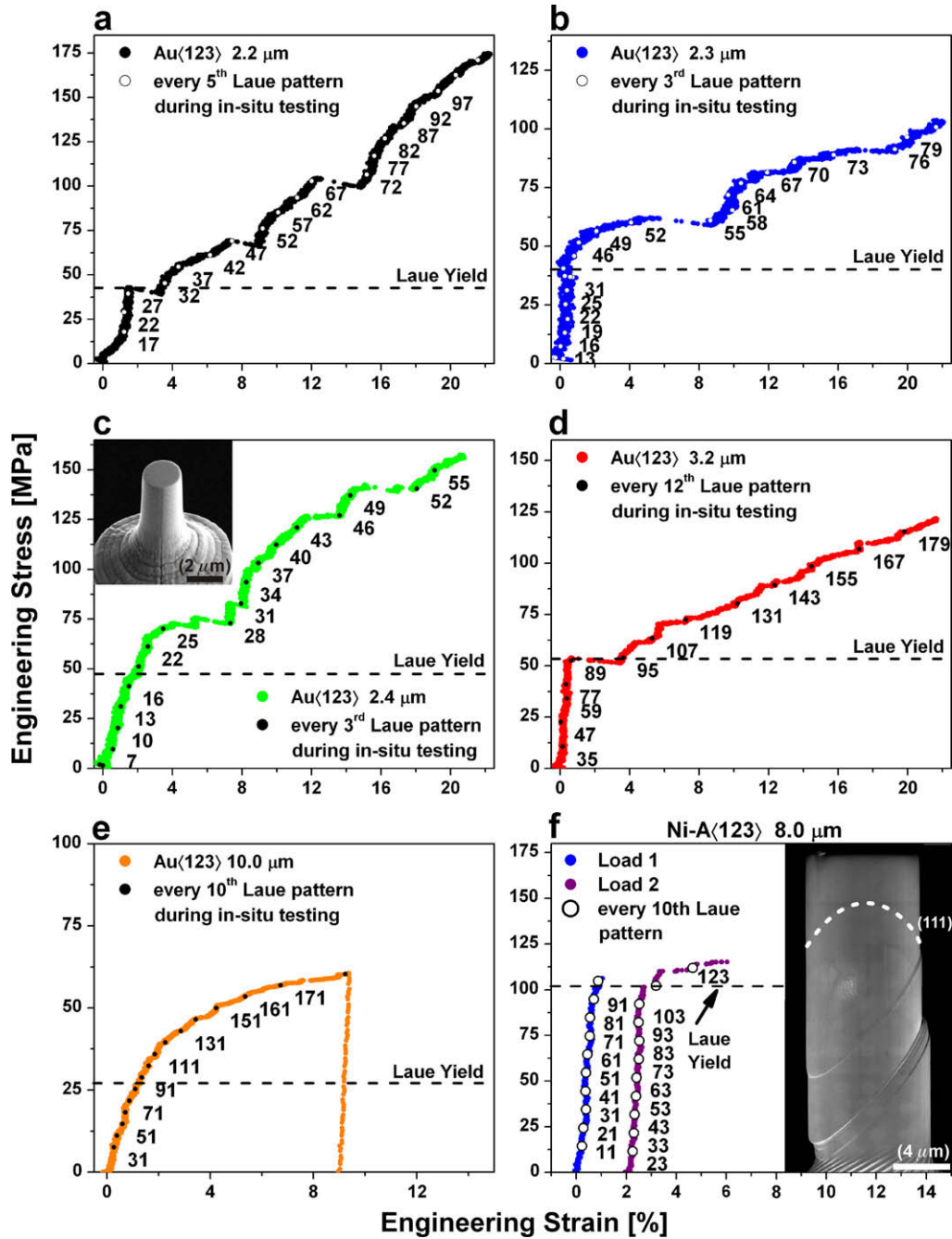


Fig. 1. (a–d) Stress–strain curves of four tested $\langle 1\ 2\ 3 \rangle$ -micropillars, (e) flow curve of a 10.0 μm $\langle 3\ 4\ 6 \rangle$ -pillar from a previous study [29], and (f) an load–unload test performed on the 8.0 μm Ni-A $\langle 1\ 2\ 3 \rangle$ -sample. The inset in (c) displays the undeformed pillar, and the deformed Ni-A is depicted as an inset in (f).

with simple geometry and approximating the response to a given local constitutive behavior in such domains under the boundary conditions imposed jointly by external and internal constraints. Of importance in this paper is the use of a crystalline elastic and plastic anisotropic constitutive law [36–39].

In conventional isotropic continuum mechanics crystallographic rotations, and hence orientation effects, do not play a role as an antisymmetric portion associated with the dyadic nature of crystallographic dislocation slip (i.e. shear only along discrete directions on discrete planes) does

not exist. This means that isotropic constitutive approaches to materials micromechanics are less useful in cases where the crystalline nature of matter plays an important role in terms of anisotropy and deformation-induced orientation changes including effects of initial orientation variations, orientation fragmentation [37], friction or tool misalignment. An overview of the different approaches to the incorporation of crystalline anisotropy into finite-element schemes is given in Refs. [36–40].

In this investigation the crystal plasticity finite-element method (CP-FEM) was used to systematically study intrinsic

sample parameters, such as the initial orientation and the evolution of deformation-induced orientation changes and strain-hardening evolution upon mechanical loading, and—most importantly—extrinsic effects, such as tool misalignment, sample geometry and contact conditions, in small-scale compression tests.

In order to describe the flow kinematics the finite deformation defined by the deformation gradient, F , is multiplicatively decomposed into two contributions, namely the elastic and rotational part of the deformation gradient, F^* , and the plastic part of the deformation gradient, F_p [36–40]. The latter quantity describes an intermediate configuration accounting only for the deformation induced by the plastic slip in the lattice, i.e. $\det F_p = 1$. The elastic and rotational portion of the deformation gradient, F^* , captures both the stretch and the rotation of the lattice. The flow rule was used in the form:

$$\dot{F}_p = L_p F_p, \quad (1)$$

and the plastic velocity gradient, L_p , as:

$$L_p = \sum_{\alpha} \dot{\gamma}_{\alpha} (m_0^{\alpha} \otimes n_0^{\alpha}), \quad (2)$$

where m_0^{α} and n_0^{α} are the orthonormal vectors describing the slip direction and the slip plane normal of the slip system α in the reference configuration, respectively. $\dot{\gamma}_{\alpha}$ describes the shear rates on the slip systems α .

The phenomenological hardening law is based on a crystal plasticity model which was suggested by Rice [41] and Peirce et al. [42,43] for the fcc lattice. The kinetic law on a slip system α follows:

$$\dot{\gamma}_{\alpha} = \dot{\gamma}_0 \left| \frac{\tau_{\alpha}}{s_{\alpha}} \right|^{1/m} \text{sign}(\tau_{\alpha}), \quad (3)$$

where $\dot{\gamma}_{\alpha}$ is the shear rate on the slip system subjected to the resolved shear stress τ_{α} having a slip resistance of s_{α} . $\dot{\gamma}_0$ and m are material parameters and stand for the reference shear rate and for the rate sensitivity of slip, respectively. The influence of any slip system β on the hardening behavior of system α is given by:

$$\dot{s}_{\alpha} = \sum_{\beta} h_{\alpha\beta} |\dot{\gamma}_{\beta}|, \quad (4)$$

where $h_{\alpha\beta}$ is referred to as the hardening matrix:

$$h_{\alpha\beta} = q_{\alpha\beta} \left[h_0 \left(1 - \frac{s_{\beta}}{s_{\alpha}} \right)^{\alpha} \right], \quad (5)$$

which empirically captures the micromechanical interaction among different slip systems. In this formulation h_0 , α and s_{α} are slip hardening parameters, which are assumed to be identical for all fcc slip systems owing to the underlying characteristic dislocation reactions. The parameter $q_{\alpha\beta}$ is taken as 1.0 for coplanar slip systems α and β , and 1.4 otherwise, which renders the hardening model anisotropic [44]. The hardening parameters in Eqs. (3)–(5) for Au and Ni were fitted from polycrystal flow curves [45].

3. Results

3.1. Mechanical testing

Fig. 1 displays the stress–strain curves for four $\langle 1\ 2\ 3 \rangle$ -Au pillars (a–d), for a $10\ \mu\text{m}$ Au $\langle 3\ 4\ 6 \rangle$ -oriented sample (e) taken from Ref. [26], and for the two successive loads of an $8\ \mu\text{m}$ $\langle 1\ 2\ 3 \rangle$ -Ni pillar (f). For the calculation of the stress of the tapered pillars, the average of the bottom and top diameters is used, as is done elsewhere in the published literature. The numbers of the recorded Laue patterns are superimposed on the stress–strain curves. The two insets show the undeformed (Fig. 1c) and deformed (Fig. 1f) pillars imaged by scanning electron microscopy (SEM). After the second loading cycle performed on the $8\ \mu\text{m}$ Ni-A sample, most of the slip lines correspond to the primary $(-1\ 1\ 1)$ slip plane; careful examination, however, also reveals a few slip lines corresponding to the $(1\ 1\ 1)$ -plane. The slope during the initial raise of the stress is very different from pillar to pillar, as also found in the literature [5,6,14,16,46–48]. These important differences make it difficult to define the yield stress at low strains [14,16], which is the reason that the stress at 5% strain [6], 10% strain [5,49] or sometimes 20% total strain [15] is used as a measure of strength.

3.2. Diffraction data

The positions of the diffraction peaks have been traced by the first-order moment of the intensity distribution and by the maximum intensity; both methods demonstrate a shift in peak position during the initial loading. Fig. 2a–c shows (in detector units) the path of the $(-2\ -2\ -2)$ Laue reflection of the Au- $2.3\ \mu\text{m}$ pillar, the $(1\ -1\ 1)$ -reflection of the Au- $4.5\ \mu\text{m}$ pillar, and the $(1\ -3\ 1)$ -reflection during the first loading cycle of the $8\ \mu\text{m}$ Ni-A pillar. An arrow marks the peak position prior to deformation. For the Au and the Ni pillars, the first movement of each diffraction peak (colored blue) is closely following one line indicated with a blue arrow, corresponding to the rotation direction expected when slip occurs on the $(1\ 1\ 1)$ -plane for Au and on the $(-1\ -1\ 1)$ -plane for Ni. Both initial rotations correspond to dislocation activity on a geometrically less favorable slip plane. The orientation of these planes is shown in Fig. 2e–f and the SF values are given in Table 1. After a certain amount of loading, an abrupt change in path of the Laue peaks is observed (indicated in red), corresponding to dislocation activity predominantly on the classically predicted slip plane, which is the $(-1\ 1\ 1)$ for both Au and Ni containing the $(-1\ 1\ 1)[1\ 0\ 1]$ slip system with the highest SF. The direction chosen by the Laue spots of the Ni pillar does not correspond with single slip on the $(-1\ 1\ 1)$ -plane but suggests a combination of the $(-1\ 1\ 1)$ and $(1\ 1\ 1)$ -plane, an observation confirmed by the SEM image (Fig. 1f). The Laue pattern number associated with the sudden change in path is indicated for all pillars, and the corresponding stresses are derived from Fig. 1. In what follows

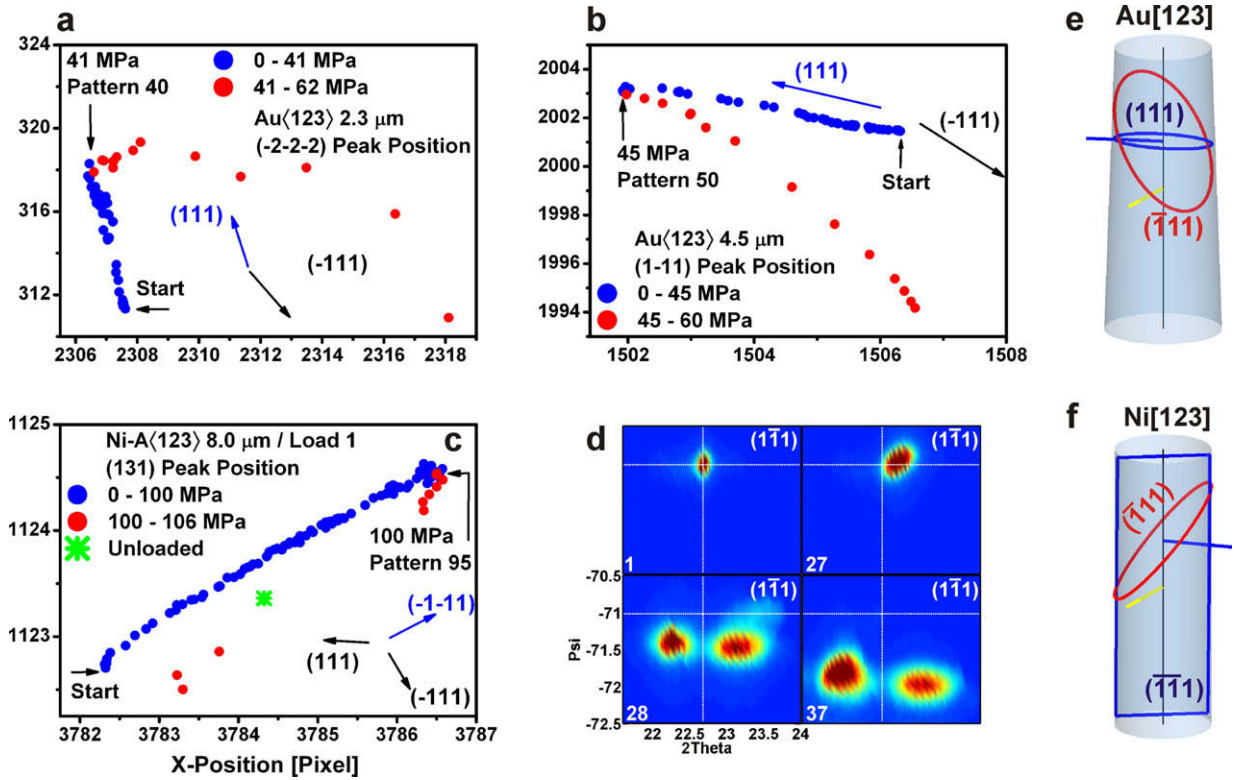


Fig. 2. (a and b) Peak movement of the $(-2 -2 -2)$ and $(1 -1 1)$ -peak of the 2.3 and 4.5 μm Au pillar, respectively, showing the change in Laue spot path; (c) the $(1 -3 1)$ Ni-A reflection traced during load 1 shown in Fig. 1d, also evidencing a change in peak movement; (d) shows the movement of the $(1 -1 1)$ -reflection of the 2.2 μm Au $\langle 1 2 3 \rangle$ -pillar in angular measurements, with the initial peak (1), the peak before the change in path (27) followed by a change in peak path and peak splitting (28) at 1.5% strain and at 4.3% strain (37), the initial peak position with a dotted cross; (e and f) in blue the initially activated low-SF plane with the corresponding rotation axis, and in red the predicted slip plane—the yellow line indicates the incoming beam axis. (Laue pattern numbering analogous to the stress–strain curves shown in Fig. 1). (For interpretation of the references to colour in this figure legend, the reader is referred to the web version of this article.)

we will define the stress at which the change between the two modes occurs as “Laue-yield” and consider this as the strength of the pillar instead of the flow stress at a fixed amount of 5% total strain.

Looking at the shape of the Laue reflection, the change in peak position is accompanied by a peak broadening during the initial loading. When a pre-existing gradient was present the broadening direction coincides with the initial streaking direction. In most of the pillars a splitting in one of the diffraction peaks is observed after the sudden change in peak path, evidencing local plasticity in the illuminated volume involving crystal polygonization and crystal rotation. The shape of the $(1 -1 1)$ Laue spot of the 2.2 μm Au pillar is pictured in Fig. 2d in angular units prior to loading (1), just before (27) and just after the sudden change in path direction (28) and at 4.3% strain (37).

Fig. 3a and b depicts the path of the $(1 -1 1)$ -reflection (in detector units) of the 2.2 μm Au $\langle 1 2 3 \rangle$ pillar for which the splitting of the Laue spot upon change in peak path is shown in Fig. 2d. Both Fig. 3a and b shows the initial path of the peak before splitting (in blue). The red path in Fig. 3a shows the path of the left-hand sub-reflection in Fig. 2d, the red path in Fig. 3b the path of the right-hand sub-reflection. The first burst measured on the stress–strain curve (Fig. 1a) seems to be related to the formation of two

substructures resulting in two diffraction peaks. One of them (a) follows, upon further deformation, the path corresponding to slip on the $(-1 1 1)$ plane, the other (b) initially behaves similarly, but subsequently follows a path in between the $(1 1 1)$ and the $(-1 1 1)$ predicted rotation directions. That the pillars are plastically deforming after the sudden change in peak path is also evidenced by the non-recoverable peak position of the Ni pillar at 106.2 MPa, unloaded shortly after the change in peak path (green spot in Fig. 2c).

Due to the high symmetry, the tested $\langle 0 0 1 \rangle$ -orientation has four planes equally oriented and thus eight slip systems with equal SFs, nevertheless a change in peak path is observed after a small amount of strain. Similar to Au $\langle 1 2 3 \rangle$, the $\langle 0 0 1 \rangle$ - and $\langle 3 4 6 \rangle$ -oriented Au micropillars show a comparable change in direction of the peak movement during the early stage of deformation. In the pillars oriented for multiple slip with eight slip systems having equal SFs, the peak path does not correspond to a distinct slip plane, but is observed to be in between the lines predicted by the Taylor model for rotation. The change in path is, however, also present, as shown in Fig. 3c for the 5.1 μm pillar, and occurs at 33 MPa. In the $\langle 3 4 6 \rangle$ -oriented pillars a $(1 -1 1)$ -rotation is first chosen, followed by the predicted $(1 -1 -1)$ system, as displayed in

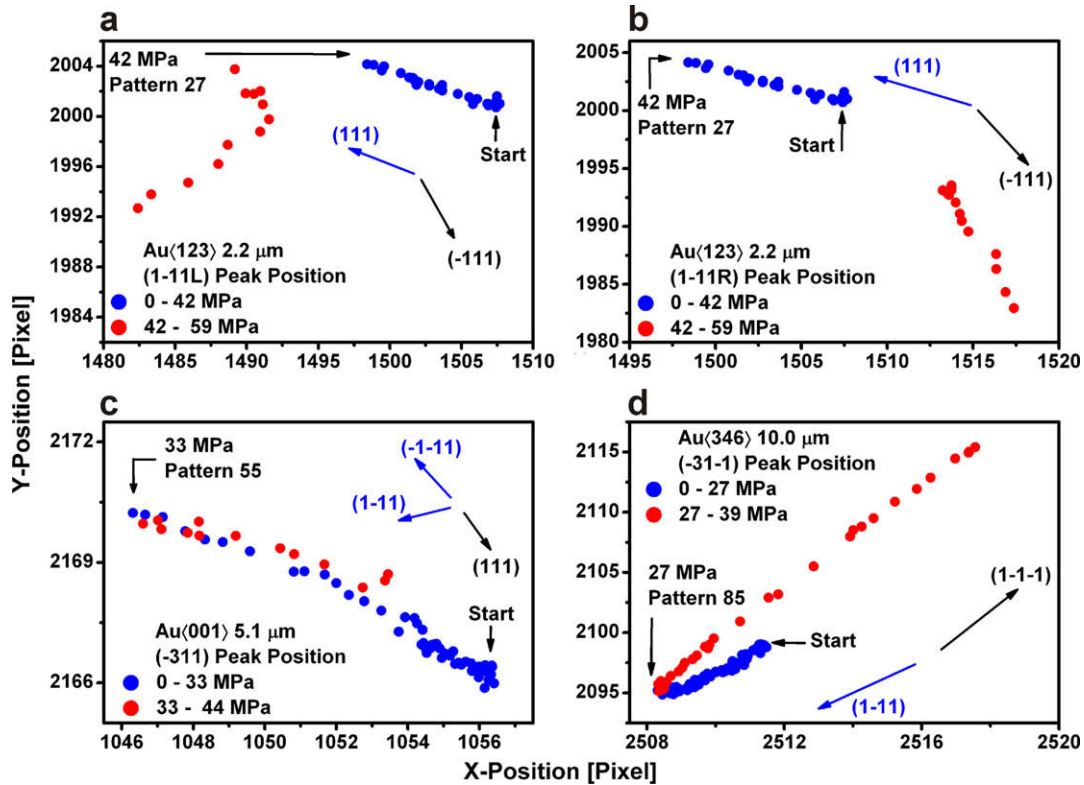


Fig. 3. Initial peak movement for the $2.2 \mu\text{m}$ Au(001) that splits in relation to the change in peak: blue indicated the path before splitting, red after splitting. (a) The red path corresponds to the left sub-Laue spot in Fig. 2d. (b) The red path corresponds to the right sub-Laue spot. Initial peak movement for (c) a $5.1 \mu\text{m}$ Au(001) and (d) a $10.0 \mu\text{m}$ Au(346) micropillar. (For interpretation of the references to colour in this figure legend, the reader is referred to the web version of this article.)

Fig. 3d. The “Laue yield” occurs at around 28 MPa for the $4.6 \mu\text{m}$ Au(346)-pillar and at 27 MPa for the $10.0 \mu\text{m}$ Au(346)-pillar.

The rotation of the vertical crystal axis was derived from the path followed by all Laue spots by means of full Laue pattern fitting and plotted in a stereographic projection. Fig. 4 displays the vertical crystal axis for the $2.4 \mu\text{m}$

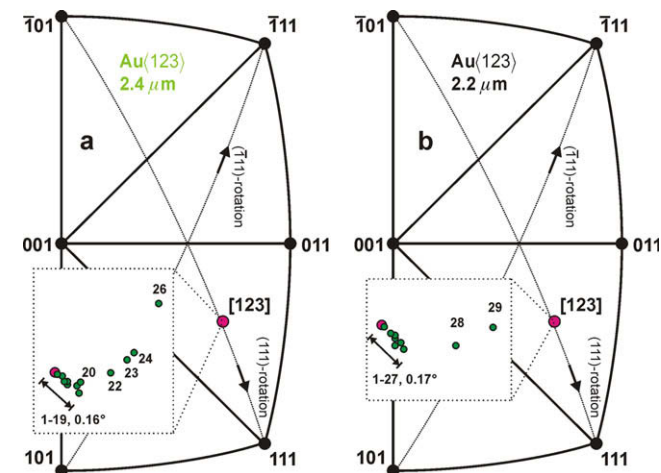


Fig. 4. Evolution of the vertical crystal axis orientation for the $2.4 \mu\text{m}$ (a) and $2.2 \mu\text{m}$ (b) Au(123)-sample, revealing initial activation of the (111)-plane. In both cases the corresponding Laue pattern numbers and the total amount of rotation are indicated.

(Fig. 4a) and $2.2 \mu\text{m}$ micropillar (Fig. 4b) in the $\langle 123 \rangle$ -orientation. The red points mark the initial orientation and the insets provide the details of its path followed during the initial loading with the corresponding numbers of the Laue patterns. Both pole figures show that initially a $0.16\text{--}0.17^\circ$ rotation is present, corresponding to dislocation activity on the geometrically non-predicted slip (111)-plane, followed by larger rotations corresponding with predominant activity on the predicted (-111) -slip plane, providing thus a similar picture as the individual peak movements.

For some samples peak splitting was evidenced prior to the “Laue yield”, which demonstrates that the “Laue yield” is still an overestimation of the onset of macroscopic plasticity. For instance, in the $8 \mu\text{m}$ Ni-B and the $4 \mu\text{m}$ Ni pillars, peak splitting is observed well before the change in peak path, at 68 and 59 MPa, respectively, instead of the corresponding 86 and 96 MPa of the “Laue yield”. Fig. 5 shows the normalized (131)-reflection of the $8 \mu\text{m}$ Ni-B sample at 0 MPa (a), 70 MPa (b), 77 (c) and at 86 MPa (d), the stress at which the “Laue yield” occurs.

3.3. Crystal plasticity FEM simulations

Since lattice rotations are a signature of constraints, CP-FEM was employed to investigate the role of tool misalignments on (123)-oriented Au and Ni pillars. CP-FEM is a

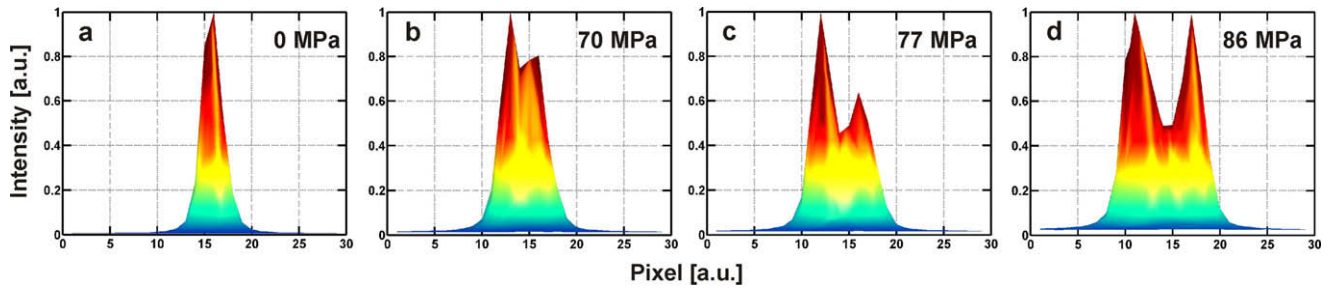


Fig. 5. $(1\ 1\ 1)$ -Peak splitting during loading prior to the “Laue yield” for the $8\ \mu\text{m}$ Ni-B pillar, showing that the “Laue yield” is still an overestimation of the onset of plasticity.

variational approach that accounts in its underlying constitutive formulation for the elastic–plastic anisotropy of crystalline matter. It is particularly suited to predicting slip activity and plastic interaction phenomena under complicated boundary conditions such as encountered in small-scale mechanical experiments [40,44,50] as it incorporates a fully tensorial description of plasticity using a viscoplastic approach. Fig. 6 shows the predicted crystallographic shear rates on all 12 slip systems for a tapered Au pillar (Fig. 6a) and a non-tapered Ni pillar (Fig. 6b) as investigated in the current in situ Laue diffraction experiments. The pillars were loaded under compression at zero friction and with a tool inclination of 2° off the ideal punch direction.

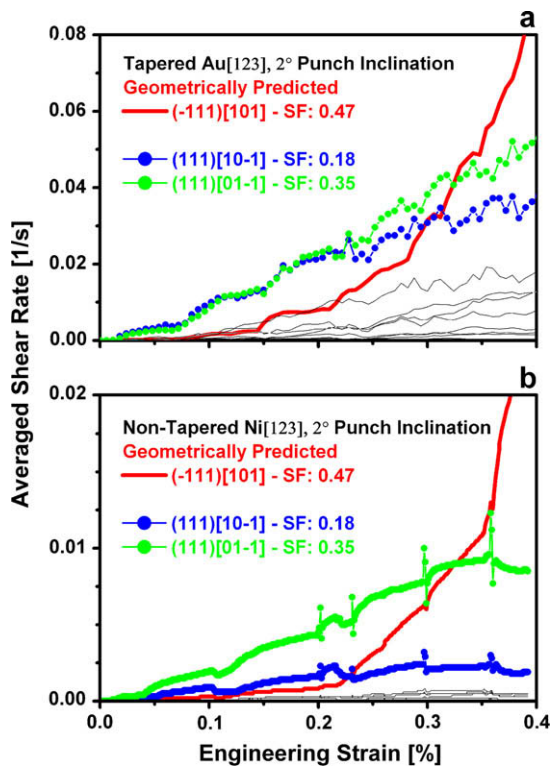


Fig. 6. Average shear rates on all 12 slip systems for the compression of micropillars of the same geometry and taper as investigated in the current experiments. The boundary conditions were compression at zero friction and tool inclination of 2° off the ideal punch direction (SF, Schmid factor). (a) Tapered Au pillar and (b) non-tapered Ni pillar.

Fig. 6 depicts the averaged shear rate as a function of engineering strain for both the investigated Au and Ni sample geometries. In both graphs the red line describes the shear rate evolution of the geometrically predicted $(-1\ 1\ 1)[1\ 0\ 1]$ slip plane, which is expected to be dominant in an ideal uniaxial compression experiment. Under a 2° tool inclination, however, both simulations show first the activity of two slip systems that are geometrically unexpected if a perfect uniaxial compressive stress state is anticipated, before the expected system finally becomes dominant, i.e. the $(1\ 1\ 1)[1\ 0\ -1]$ system with SF = 0.35 and the $(1\ 1\ 1)[0\ 1\ -1]$ system with SF = 0.18. Beyond 0.3% strain the geometrically predicted slip system reaches the highest shear rate. This prediction matches the experimental observation of plasticity on an unexpected slip plane observed for both types of pillars, although the transition to the expected system occurs at a smaller strain in the simulation. Fig. 6 also shows that the activity on the two low-SF slip systems is more important in the tapered pillar geometry (Fig. 6a) compared to the untapered one (Fig. 6b). For the single slip oriented and tapered Au pillars, CP-FEM predicts the initial activation of the same two slip systems on the $(1\ 1\ 1)$ -plane as those observed in the in situ Laue experiment (Figs. 2a,b and 4).

4. Discussion

Au pillars with a sidewall taper and Ni pillars without taper both synthesized using FIB were compressed in situ during Laue diffraction at the MicroXAS beamline of the SLS. Eight Au and three Ni pillars with diameters between 2 and $10\ \mu\text{m}$ were oriented for single slip ($\langle 1\ 2\ 3 \rangle$, $\langle 3\ 4\ 6 \rangle$) and two Au pillars were oriented for multiple slip ($\langle 0\ 0\ 1 \rangle$). The initial diffraction peaks of all single slip oriented Au pillars exhibit continuous streaks which can be interpreted in terms of strain gradients. The diffraction peaks of two of the Ni pillars ($8\ \mu\text{m}$ (B) and $4\ \mu\text{m}$) evidences minor peak splitting, pointing to the presence of small angular misorientations. The $3\ \mu\text{m}$ Au $\langle 1\ 2\ 3 \rangle$ -pillar contains a misorientation in the lower part of the pillar [24]. The presence of strain gradients has been associated with the FIB synthesis procedure [23] and the effect of the latter has been recently discussed for body-centered cubic pillars [48].

For all crystallographic orientations, a sudden change in peak path is observed, which reflects a distinct change in the rotational mode or activation of different slip planes. The stress corresponding to the change in peak path is termed “Laue yield” and can be considered as the onset of percolative slip, after which the geometrically predicted slip plane becomes active. For the single slip oriented Au and Ni samples the slip planes activated first correspond to low-SF planes. The stresses at which the “Laue yield” is observed can be linked to the stress–strain curves shown in Fig. 1. In each graph in Fig. 1a dashed horizontal line indicates the stress at which the “Laue yield” occurred. These graphs clearly indicate that the “Laue yield” does not necessarily correspond to a unique feature in the stress–strain curve: sometimes it corresponds to a strain burst (Fig. 1a and c), and sometimes to a distinguishable change in slope between what resembles the elastic loading regime and the strain-hardening regime (Fig. 1b and c), but it has also been observed to occur along the alleged initial linear part of the stress–strain curve (Fig. 1c and e).

Table 2 provides, for all pillars analyzed, the “Laue yield” stress and corresponding total strain values, the amount of rotation observed before the classical predicted slip system sets in, and the stress corresponding to 5% strain as is often used in the literature. All Au pillars with a diameter of 2 μm show a “Laue yield” between 40 and 48 MPa which is considerably lower than the value of the flow stress at 5% strain. There is no clear relation to the corresponding strain, but when larger strains are measured at the “Laue yield”, the corresponding amount of rotation related to activity on the low-SF plane increases.

For the 4.6 μm pillar of the $\langle 3\ 4\ 6 \rangle$ -orientation no rotation could be derived within the scatter of the technique due to the fact that the beam was exceptionally positioned in the lower part of the pillar, resulting in overlapping diffracted intensities from substrate and pillar, which cannot be separated for all peaks during full pattern fitting. For the same size of pillars, the highest “Laue yield” stress is comparable to that measured for the 2 μm pillars and corresponds to the pillar for which also the highest amount of rotation is observed. Note that in the absence of important initial rotation on a low-SF plane, the “Laue yield” stress corresponds with the value measured for a 10 μm pillar, which is well within the limits measured for bulk Au. The scatter observed among the three Ni pillars does not allow any conclusion to be derived concerning the relation between yield and initial rotation; nor is it possible to confirm the “smaller is stronger” trend suggested at 5% strain. It is important to mention that for the 8 μm Ni-B and the 4 μm Ni samples, peak splitting is observed well before the change in peak path. This means that the “Laue yield” is still an overestimation of the onset of percolative slip when the pillar deforms already plastically in the first mode. The advantage of this definition of yield is, however, that it is based on a physical criterion, i.e. the onset of deformation as predicted for uniaxial compression constraints, and that it approaches as close as possible the onset of percolative slip.

Fig. 7 shows the “Laue yield” of all Au pillars vs. the square root of the pillar diameter and the values reported for Au in Ref. [6], demonstrating that the flow stress taken at 5% strain is between 40% and 120% higher than the stress at “Laue yield”. The strains corresponding to the “Laue yield” range between 0.2% and 2.3% as detailed in Table 2. Higher values in “Laue yield” coincide in general with larger rotations of the crystal axis before the predicted dominating slip system with the highest SF is finally activated. Because crystal rotations are observed at strains well below 5%, the strength which is reported in the literature and used to support the “smaller is stronger” paradigm has to be assigned in part to strain hardening. Note that the “Laue yield” is expected eventually to be sensitive to pre-existing defects in the pillar prior to deformation. In other words, some of the values reported in Fig. 3 might contain a strength contribution as a result of a pile-up effect. This is, for instance, the case for the 3 μm Au $\langle 1\ 2\ 3 \rangle$ pillar, which has a misorientation at the pillar base [24].

In situ Laue diffraction demonstrates the existence two deformation regimes in FIB single-crystal fcc pillars. The first one corresponds to the activity on slip systems different from those that are geometrically predicted for uniaxial compression (highest SF for anticipated ideal compression conditions). The second one is characterized by the constraints imposed by uniaxial compression. The first deformation regime must be associated with the boundary conditions of the test, i.e. the presence of an initial strain gradient in FIB pillars and/or unavoidable small tool misalignments.

Both CP-FEM simulations (Fig. 6) show the activity of two slip systems that are geometrically unexpected if a perfect uniaxial compressive stress state is anticipated, before the expected system finally becomes dominant. This prediction matches the experimental observation of plasticity on an unexpected slip plane observed for both types of pillars, although the transition to the expected system occurs at a smaller strain in the simulation. This might be due to a rel-

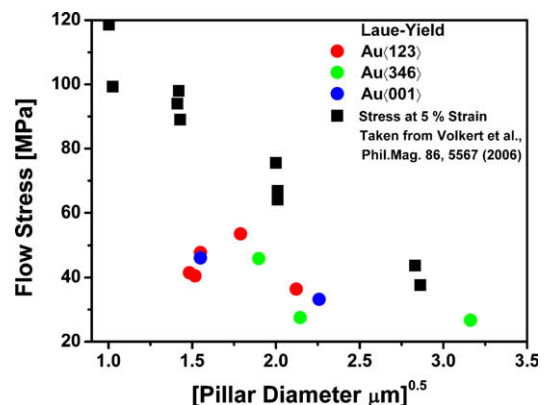


Fig. 7. Hall–Petch plot showing the “Laue yield” for all 10 Au samples as a function of the square root of the diameter. Black squared data points are taken from Ref. [6] and were derived at 5% strain from stress–strain curves of single slip oriented Au pillars.

atively simple constitutive description of hardening in the model. Independent of whether it is the initial strain gradient, the unavoidable small misalignments between indenter and pillar, or the interplay between both effects, the dislocations on the expected slip system activated after the “Laue yield” will interact with those resulting from slip activity on the unexpected preceding slip systems, leading to cross-hardening.

5. Summary

Laue diffraction analysis supported by CP-FEM calculations demonstrate that in a microcompression experiment plasticity starts on slip systems that are geometrically not predicted for uniaxial compression, but can be understood by taking into account the complete stress tensor representing more complex boundary constraints. Crystal rotation and the formation of substructures occur even at very small strains. Therefore, when using the flow stress at 5% strain or higher, the “smaller is stronger” paradigm observed for 1–10 μm fcc FIB pillars is to a great extent due to size-dependent strain hardening, i.e. the evolution of the microstructure during deformation, and not to a size dependence of the initial strength of the single-crystal pillar. The current results suggest the use of microfocused X-ray facilities at synchrotrons in conjunction with CP-FEM analysis to further explore the “smaller is stronger” paradigm and the early stages of strain hardening.

Acknowledgments

We thank M.D. Uchic for providing the Ni micropillars and M. Willmann and C.N. Borca from the MicroXAS beam line of the Swiss Light Source for technical support. Furthermore are we grateful for the help of S. Brandstetter during beamtime. H.V.S. thanks the Swiss National Science Foundation (No. SNF-2100-065152.01, SNF-200020-116283/1), the European Commission (6th framework) for financial support of the project NANOMESO and Hysitron Inc. for supporting the TriboScope© implementation.

References

- [1] Uchic MD, Dimiduk DM, Florando JN, Nix WD. *Science* 2004;305:986.
- [2] Juan JMS, No ML, Schuh CA. *Adv Mater* 2008;20:272.
- [3] Frick CP, Orso S, Arzt E. *Acta Mater* 2007;55:3845.
- [4] Mara NA, Bhattacharyya D, Dickerson P, Hoagland RG, Misra A. *Appl Phys Lett* 2008;92.
- [5] Greer JR, Nix WD. *Phys Rev B* 2006;73:245410.
- [6] Volkert CA, Lilleodden ET. *Philos Mag* 2006;86:5567.
- [7] Bei H, Shim S, Pharr GM, George EP. *Acta Mater* 2008;56:4762.
- [8] Buzzi S, Dietiker M, Kunze K, Spolenak R, Löffler JF. *Philos Mag* 2009;89:869.
- [9] Hertzberg RW. *Deformation and fracture mechanics of engineering materials*. New York: John Wiley; 1995.
- [10] ASTM. *Standard test methods for tension testing of metallic materials*. E8-04. West Conshohocken (PA): ASTM International; 2004.
- [11] Kocks UF, Mecking H. *Prog Mater Sci* 2003;48:171.
- [12] Hall EO. *Proc Phys Soc Lond Section B* 1951;64:747.
- [13] Petch NJ. *J Iron Steel Inst* 1953;174:25.
- [14] Frick CP, Clark BG, Orso S, Schneider AS, Arzt E. *Mater Sci Eng: A* 2008;489:319.
- [15] Kiener D, Motz C, Schoberl T, Jenko M, Dehm G. *Adv Eng Mater* 2006;8:1119.
- [16] Dimiduk DM, Uchic MD, Parthasarathy TA. *Acta Mater* 2005;53:4065.
- [17] Horstemeyer MF, Baskes MI, Godfrey A, Hughes DA. *Int J Plast* 2002;18:203.
- [18] Levine LE, Larson BC, Yang W, Kassner ME, Tischler JZ, Delos-Reyes MA, et al. *Nat Mater* 2006;5:619.
- [19] Jakobsen B, Poulsen HF, Lienert U, Almer J, Shastri SD, Sorensen HO, et al. *Science* 2006;312:889.
- [20] Margulies L, Winther G, Poulsen HF. *Science* 2001;291:2392.
- [21] Bei H, Barabash RI, Ice GE, Liu W, Tischler J, George EP. *Appl Phys Lett* 2008;93:071904.
- [22] Ice GE, Barabash RI. In: Nabarro FRN, Hirth JP, editors. *Dislocation in solids*, vol. 13. Amsterdam: Elsevier; 2007 [chapter 79].
- [23] Maass R, Grolimund D, Van Petegem S, Willmann M, Jensen M, Van Swygenhoven H, et al. *Appl Phys Lett* 2006;89:151905.
- [24] Maass R, Van Petegem S, Zimmermann J, Borca CN, Van Swygenhoven H. *Scrip Mater* 2008;59:471.
- [25] Maass R, Van Petegem S, Grolimund D, Van Swygenhoven H, Uchic MD. *Appl Phys Lett* 2007;91:131909.
- [26] Maass R, Van Petegem S, Van Swygenhoven H, Derlet PM, Volkert CA, Grolimund D. *Phys Rev Lett* 2007;99:145505.
- [27] Maass R, Van Petegem S, Grolimund D, Van Swygenhoven H, Kiener D, Dehm G. *Appl Phys Lett* 2008;92:071905.
- [28] Yang W, Larson BC, Tischler JZ, Ice GE, Budai JD, Liu W. *Micron* 2004;35:431.
- [29] Chung JS, Ice GE. *J Appl Phys* 1999;86:5249.
- [30] Barabash RI, Ice GE, Walker FJ. *J Appl Phys* 2003;93:1457.
- [31] Taylor GI. *Proc Roy Soc Lond Ser A-Contain Pap Math Phys Char* 1927;116:16.
- [32] Hosford WF. *The mechanics of crystals and textured polycrystals*. Oxford: Oxford University Press; 1993.
- [33] Tamura N, MacDowell AA, Spolenak R, Valek BC, Bravman JC, Brown WL, et al. *J Synchrotron Radiat* 2003;10:137.
- [34] Uchic MD, Dimiduk DA. *Mater Sci Eng A* 2005;400:268.
- [35] Gerberich WW, Yu W, Kramer D, Strojny A, Bahr D, Lilleodden E, et al. *J Mater Res* 1998;13:421.
- [36] Ma A, Roters F, Raabe D. *Int J Solids Struct* 2006;43:7287.
- [37] Ma A, Roters F, Raabe D. *Acta Mater* 2006;54:2181.
- [38] Raabe D, Sachtleber M, Zhao Z, Roters F, Zaefferer S. *Acta Mater* 2001;49:3433.
- [39] Kalidindi SR, Bronkhorst CA, Anand L. *J Mech Phys Solids* 1992;40:537.
- [40] Zaafarani N, Raabe D, Singh RN, Roters F, Zaefferer S. *Acta Mater* 2006;54:1863.
- [41] Rice JR. *J Mech Phys Solids* 1971;19:433.
- [42] Peirce D, Asaro RJ, Needleman A. *Acta Metall* 1983;31:1951.
- [43] Peirce D, Asaro RJ, Needleman A. *Acta Metall* 1982;30:1087.
- [44] Raabe D, Ma D, Roters F. *Acta Mater* 2007;55:4567.
- [45] Kovacs I, Voros G. *Int J Plast* 1996;12:35.
- [46] Ng KS, Ngan AHW. *Acta Mater* 2008;56:1712.
- [47] Greer JR, Weinberger CR, Cai W. *Mater Sci Eng A* 2008;493:21.
- [48] Shim S, Bei H, Miller MK, Pharr GM, George EP. *Acta Mater* 2009;57:503.
- [49] Kiener D, Grosinger W, Dehm G. *Scrip Mater* 2009;60:148.
- [50] Weber F, Schestakow I, Roters F, Raabe D. *Adv Eng Mater* 2008;10:737.